ilmedia

Technische Universität Ilmenau

Deng, Zhichao; König, Jörg; Cierpka, Christian

A combined velocity and temperature measurement with an LED and a low-speed camera

A combined velocity and temperature measurement with an LED and a low-speed camera

Zhichao Deng* , **Jörg König** and **Christian Cierpka**

Institute of Thermodynamics and Fluid Mechanics, Technische Universität Ilmenau, Am Helmholtzring 1, 98693 Ilmenau, Germany

E-mail: zhichao.deng@tu-ilmenau.de

Abstract

Microfluidic devices are governed by three-dimensional velocity and temperature fields, and their boundary conditions are often unknown. Therefore, a measurement technique is often desired to measure both fields in a volume. With astigmatism particle tracking velocimetry (APTV) combined with luminescence lifetime imaging, the temperature and all velocity components in a volume can be measured with one optical access. While the three-dimensional particle position is determined by evaluating the shape of the corresponding particle image, the temperature measurement relies on estimating the temperature-dependent luminescence lifetime derived from particle images on two subsequent image captures shortly after the photoexcitation. For this, typically a high-energetic pulsed laser is required to ensure a high signal-to-noise ratio. However, it can also cause additional heating of the fluid. We show that this problem is solved by replacing the pulsed laser with an LED. To compensate for the lower power provided by the LED, we adapted the timing schedule and vastly extended the illumination time and the exposure time for both image captures. In addition, we were able to replace the typically used high-speed camera with an ordinary double-frame camera. In this way, very low measurement uncertainties on all measured quantities can be achieved while keeping the temperature of the fluid unaffected. Random errors dominate within the two focal planes of APTV, yielding a standard deviation of the temperature of individual particles of about 1 °C only. The measurement error caused by the movement of tracer particles during the much longer illumination and exposure time were found to be acceptable when the measured velocity is low. With the circumvention of light-source induced heating and the lower cost of hardware devices, the adapted approach is a suitable measurement technique for microfluidic related research.

---

* Author to whom any correspondence should be addressed.

(Some figures may appear in colour only in the online journal)

1. Introduction

Microfluidic devices and techniques are widely used in a variety of biological or chemical related disciplines, e.g. biomimetics, drug discovery, cell analysis [1], chemical and enzymatic reactions [2], material synthesis [3], tissue engineering [4], among others. In many application scenarios, temperature change and fluid flow occur simultaneously in all three spatial dimensions, and both of them play critical roles [5]. For instance, the temperature of microfluidic direct methanol fuel cells has a large effect on the start-up time [6]. Another example would be the flow which can occur due to the Marangoni convection in the close vicinity of microelectrodes [7]. Furthermore, during the handling of living cells in microfluidic devices employing surface acoustic waves (SAW), the accompanying acoustothermal heating needs to be either prevented [8] or utilized [9]. Therefore, a combined three-dimensional temperature and velocity distribution measurement inside a microfluidic device is necessary for its design and application.

A variety of optical measurement techniques based on the imaging and tracing of small temperature-sensitive particles suspended in the fluid have been proposed in the past two decades [10–12]. By using sequential imaging of the tracer particles, the velocity was generally measured by estimating the most probable displacement of several particles (particle image velocimetry, PIV) or tracking the path lines of individual particles (particle tracking velocimetry, PTV). The temperature can be measured by utilizing the principle of luminescence thermometry incorporating luminescent materials to the tracer particles. Different temperature-sensitive luminescence features like spectral shift, lifetime, bandwidth, and so on can be used for the temperature measurement [13].

Among all these measurement methods, astigmatism particle tracking velocimetry combined with luminescence lifetime imaging (APTV & LLI) is a strong candidate for measurements in the microscopic environment [14]. With this technique, all three velocity components in three dimensions can be measured using only one camera. The measurement of the velocity components in the lateral direction perpendicular to the optical axis (hereinafter referred to as x- and y-directions) was done by following the change in the centroid location of the particle images. The measurement on the additional z-direction was enabled by using the astigmatism effect induced by a cylindrical lens in front of the camera sensor. In this way, spherical tracer particles produce elliptical images on the camera sensor, depending on their depth position. Their z-coordinate can be associated with the width and height of the elliptical particle image (AX, AY) [15, 16].

The temperature measurement is realized by applying the rapid lifetime determination approach [17] on the tracer particles dyed with the luminescent compound europium (III) thenoyltrifluoroacetonate (EuTTA). With two frames captured shortly (several µs) after the excitation of photoluminescence, for every individual particle image, the luminescence lifetime τ of the dye can be expressed as a function of the ratio between the intensities on the two frames $R := I_2/I_1$. The lifetime τ is temperature-sensitive. Hence, the relationship between temperature T and intensity ratio R can be determined with a calibration. Since τ is an inherent property of the dye, it is robust against lots of extrinsic factors like unevenly distributed illumination and the effect of photobleaching.

Typically, a high-speed camera with a frame rate in the kHz range is mandatory for the LLI measurement because at least two frames must be acquired before the photoluminescent intensity becomes too weak. Recently, Abram *et al* [18] demonstrated that even though the high-speed camera was replaced by a low frame rate gated interline transfer CCD camera operating in double-frame mode, the temperature can still be measured with sub-°C precision. However, like in most of the reported luminescence thermometry methods, in their work, a high-energetic pulsed laser was used to provide a strong excitation. In the case of small volumes or stagnant fluid this may cause unwanted heating of the fluid. Even though the energy of the light will be transmitted through the fluid or be transferred to the photoluminescence, a large portion of the energy can be absorbed by the fluid, leading to an increase of the temperature and thus changing boundary conditions. In many cases, the volume of the measured fluid was relatively large or the fluid was flowing. Therefore, the temperature rise caused by the laser was small and usually neglected. However, often in microfluidic research, the temperature measurement is performed in a small volume of fluid, either in a quiescent state or accompanied by very low velocities with laminar flow conditions. In this case, the light source induced heating has to be considered. For instance, significant heating was found during the characterization of a SAW tweezer to be used for the analysis of biological samples [19, 20]. To avoid the light source induced heating, we replace the pulsed laser with an LED with much lower power. To compensate for the low excitation intensity, we vastly extended the excitation pulse length and the camera's exposure time. In addition, the excitation coincides with the exposure of the first frame. With this different timing strategy, the high-speed CMOS camera can be replaced by a low-speed double-frame camera. In addition, the use of a low-power LED and a low-speed camera lowers the cost of the measurement setup significantly.

However, with the new timing strategy, the relationships between temperature T, luminescence lifetime τ of the phosphorescent dye and intensity ratio R are different and will be analyzed in the following. Besides, measurement biases caused by photobleaching and degradation of the luminescent dye due to high temperatures are carefully evaluated. It is shown that these can either be neglected during measurements or corrected with an appropriate data processing in calibration measurements. Furthermore, we considered an additional aspect of the combined measurement technique: the dependency of the temperature measurement and the velocity measurement on each other. After all these measures were taken, we conducted measurements on some particles in the aforementioned SAW tweezer setup. The light source induced heating was avoided. Temperature and locations of these particle were measured with a low uncertainty, showing the great potential of this technique in microfluidics related applications.

2. Experimental setup and data processing

2.1. Measurement setup

A schematic of the measurement setup replacing the high-energetic pulsed laser with an LED and the high-speed camera with a low-speed double-frame camera is given in figure 1. Depending on the demand, different microfluidic devices can be fixed on a translation stage and observed by an inverse microscope (Axio Observer 7, Zeiss GmbH). Luminescent tracer particles (Surflay Nanotec GmbH) are suspended in the fluid and dispensed on either a glass slice or a substrate made of $LiNbO_3$ necessary for SAW generation. They have a diameter of 10 μm, are made of PMMA, and dyed with EuTTA. Either deionized water or a water-glycerol mixture is used as a carrying fluid. For illumination, an LED with a central wavelength of 365 nm (Solis365C, Thorlabs Inc.) is used. The light beam is reflected into the microscope by a long-pass dichroic mirror (86-330, Edmund Optics) with a cut-on wavelength of 409 nm. It is focused by the objective lens (20× magnification, NA = 0.4, Plan-Neofluar, Zeiss GmbH) to excite the photoluminescence of the EuTTA dye. The emitted light is detected in backward direction, transmitted through the dichroic mirror and further filtered by a long-pass filter (FELH0550, Thorlabs Inc.) with a cut-on wavelength of 550 nm, since the emission peak of the dye is about 615 nm [21]. A cylindrical lens with a focal length of 250 mm is placed approximately 40 mm in front of the sensor of the camera to cause astigmatism and realize the measurement of the depth position. Images are captured by the sCMOS camera (2160 × 2560 pixel, Imager sCMOS, LaVision GmbH) with double-frame functionality. Sample images can be found in the supplementary. With this specific setup, the size of the FOV was approximately $830 \times 835\,\mu m^2$. An average scaling factor of 0.384 μm pixel^{-1} in x-direction and 0.326 μm pixel^{-1} in y-direction was determined. It has to be noted, that the scaling factors differ due to the curvature of the cylindrical lens in just one direction. A programmable timing unit (PTU X, LaVision GmbH) and a commercial software (DaVis 10, LaVision GmbH) were used to control the

trigger sequence and capture images. For the measurements with the $LiNbO_3$ substrate an additional polarizer was used to block the extraordinary image due to the birefringent materials. This polarizer additional lowers the SNR and is not necessary for measurement through the glass.

2.2. Microfluidic devices

As mentioned in the introduction, measurements were conducted on a SAW tweezer setup. In the upper-right corner of figure 1, one can see that it mainly consists of a microfluidic chamber bonded on the $LiNbO_3$ substrate. The microfluidic chamber has a volume of 120 nl ($1200 \times 1200 \times 88\,\mu m^3$) and four inlets/outlets at the corners. On the substrate, two pairs of interdigital transducers were arranged orthogonally, such that SAW can be generated when a RF-signal with the resonance frequency is applied on them. For the calibration measurement, a temperature controller (TEC 1092, Meerstetter Engineering GmbH) was used. As can be seen on the schematic shown in figure 2, it was mounted on a linear translation stage which can move in z-direction. The temperature of a Peltier element (24×24 mm^2) was measured by a PT100 sensor ($2 \times 2 \times 1$ mm^3) and controlled by a PID control loop. For the measurement investigating the measurement uncertainty caused by the movement of tracer particles, experiments were conducted on a pressure driven Poiseuille flow in a commercial micro-channel slide (μ-Slide I$^{0.2}$ Luer, ibidi) with a long straight micro channel and has a cross-section of $200 \times 5000\,\mu m^2$.

2.3. Measurement principle

The measurement of 3D location (x, y, z) is done following the standard approach of APTV measurement. The x- and y-coordinates on the image plane are determined by the centroid of the particle images, given by the peak location of the cross-correlation function between the ideal Gaussian-like image and the actual particle image. The z-coordinate is associated with the particle image width and height (AX, AY), which are derived from the edge of the particle image defined as the location where the auto-correlation function decreases to a specific threshold [16, 22]. A calibration needs to be carried out to map the image coordinates to physical coordinates. The particle suspension is first dispensed on a glass slide and fixed on the translation stage on top of the microscope. After a certain waiting time, the particles are sedimented on the surface of the glass slide. Traversing the objective lens, particle images of different heights can be taken. Their (AX, AY) can be plotted on one diagram, forming a signature 'C' shape calibration curve as depicted in figure 3. In this way, the z-coordinates are continuously mapped to different locations on the calibration curve in the AX–AY space. During the measurement, by looking for the unique point on the calibration curve that has the shortest Euclidean distance to the measured data, the relevant z-coordinate can be obtained with low uncertainty [23].

As for the measurement of the temperature T, the data processing approach also remains unchanged compared to the standard approach. We also applied the same assumption that
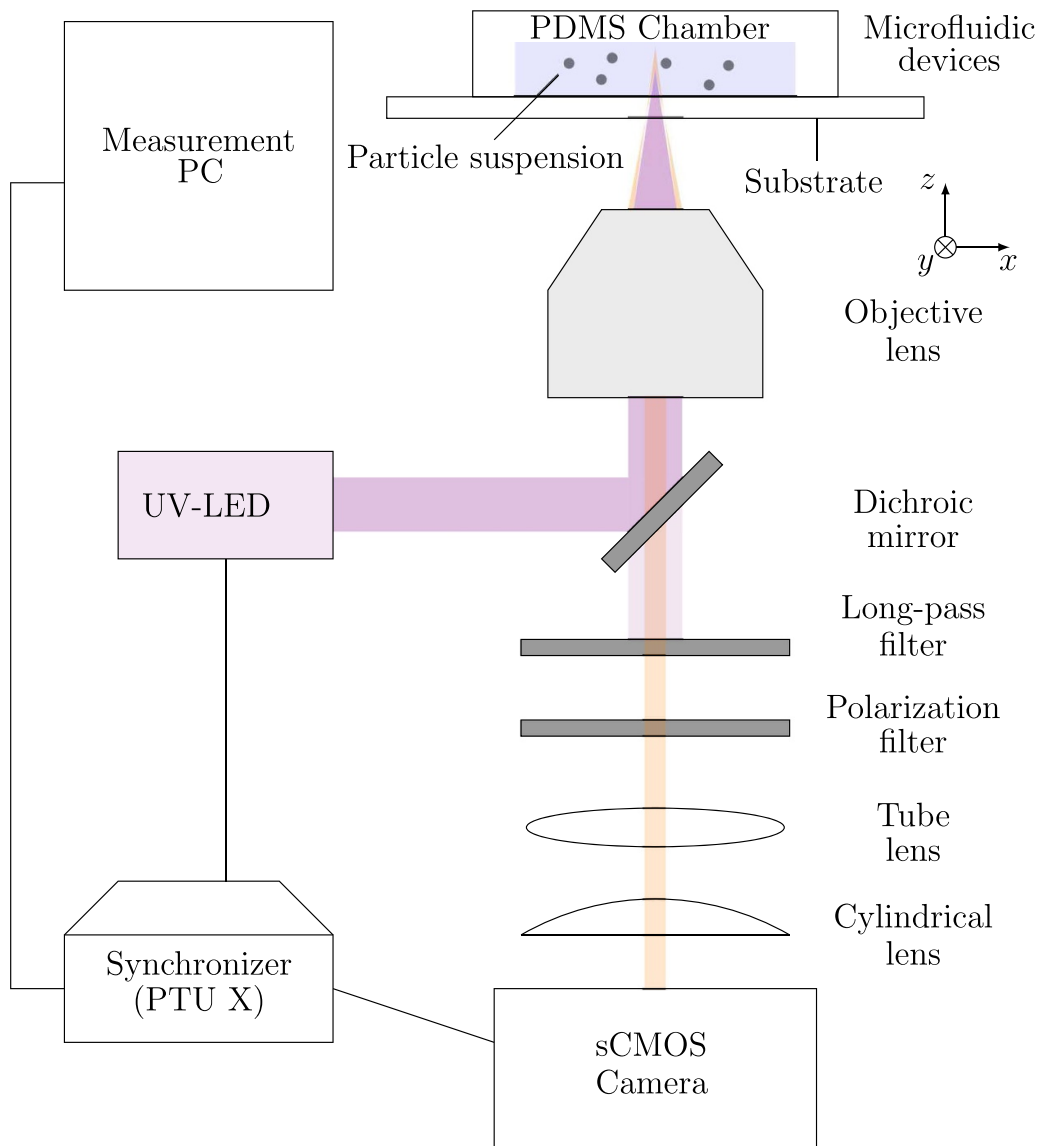
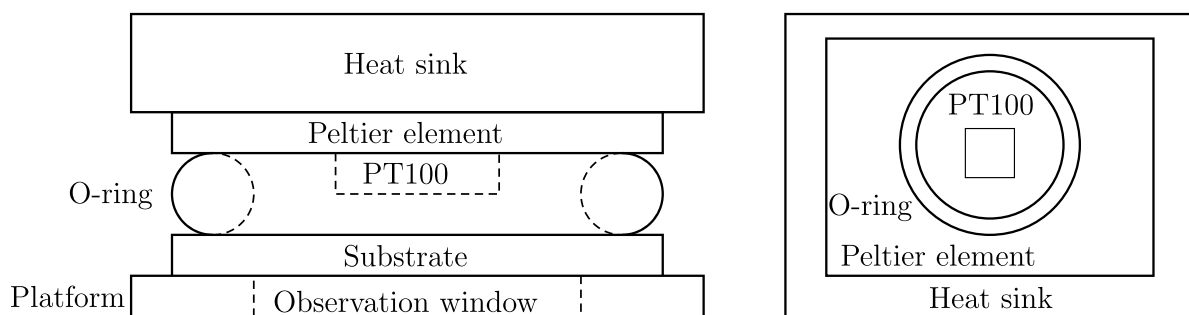**Figure 1.** A schematic of the measurement setup.

Figure 2. A sketch of the calibration stage, the front view on the left and the view from the substrate surface to the top on the right, for illustration purpose, dimensions not to scale.

the grayscale distribution of the particle image is subject to a 2D Gaussian distribution, including an offset term standing for the background noise. After the fitting, the intensity amplitude I of the 2D Gaussian is used as an indicator for the intensity of the particle image.

However, there is a fundamental change in the timing schedule compared to the conventional one depicted in the upper part of figure 4. In the adapted configuration shown in the lower part of this figure, a much longer pulse length for the photoluminescence excitation was applied. Furthermore, the
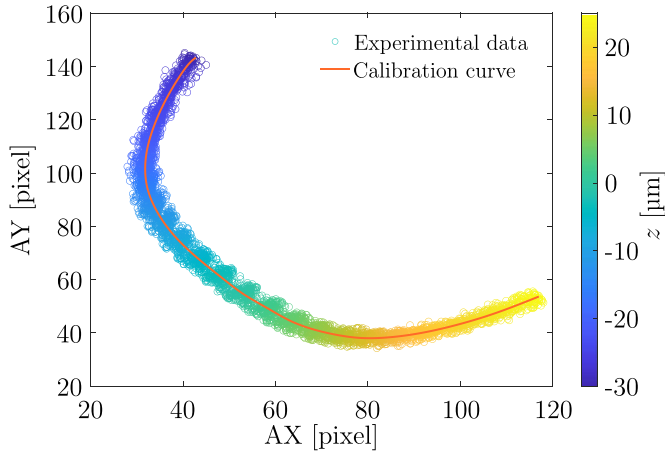
Figure 3. Calibration curve for the APTV measurement in *AX–AY* space with the measured *z*-coordinates represented by the different colors.

triggering of the exposure of frame 1 was shifted ahead and fully aligned with the excitation phase. The exposure time for frame 1 was set to be 800 μs in the current setup. The exposure of frame 2 started after a very short inter-frame gap of ∼120 ns and lasted for 10 ms, covering the whole emission phase. With a much longer integration time, the signal-to-noise ratio of the image was hugely improved despite the much weaker single pulse energy of the excitation provided by the LED. With this adaptation, the relationship between *R* and *τ* given in the [14] with the form of $R = e^{(t_1 - t_2)/\tau}$ does not hold any more. A new expression needs to be derived for the long time photoexcitation. For this, we assumed that light source delivers constantly a unit amount of the excitation photon flux Φ_i in every unit time step t_i, which gives rise to a unit portion of luminescence signal ϕ_0 decaying along time. With these assumptions, another expression for $R(\tau)$ is derived to be:

$$R(\tau) = \frac{1 - e^{-t_{exp}/\tau}}{t_{exp}/\tau - (1 - e^{-t_{exp}/\tau})}. \qquad (1)$$

Detailed derivation is provided in the supplementary information. In this way, with a given excitation and exposure time of the first frame t_{exp}, *R* can be expressed as a single variable function of *τ*, regardless of the intensity-related variables. Therefore, the estimation of *R* reserves the beneficial property of the conventional timing schedule, that it is robust against the spatial unevenly distributed illumination intensity.

However, we found a dependency of *R* on the current applied to the LED, which influences the intensity of the particle images. In figure 5, at a constant temperature the ensemble average of *R* decreases from 0.446 to 0.364 with the applied current increasing from 500 mA to 4500 mA. It might be caused by the invalidation of the mono-exponential law of the photoluminescence decay [24]. Nevertheless, for a certain applied current, the very low standard deviation of *R* implies that such a dependency can be well circumvented when we apply the same current to the LED to ensure an almost identical global illumination condition during the measurement and the calibration.

2.4. Temperature calibration

For the calibration for the temperature measurement, the calibration stage described in section 2.2 was used. The void formed by the substrate and the O-ring was filled with the particle suspension. The Peltier element was controlled to provide a periodically oscillating set temperature T_s. It was also measured by the PT100 sensor, recorded by the controlling software at a sample rate of 1 Hz, and regarded as the ground truth value. In the meantime, an image sequence was recorded with a frame rate of 10 Hz. For the recording preparation, the camera view was beforehand traversed in *xy*-plane to find the location where enough particles could be found in the FOV. Also, the objective lens was traversed along *z*-direction to roughly locate particles around the center of the measurement volume. After the recording, the spatial average intensity ratio $\overline{R}$ was evaluated on every double-frame image in a certain time step. The set temperature T_s was matched to the $\overline{R}$ assuming that they are inversely correlated. The detailed aligning process is explained in the supplementary. After that, $\overline{R}$ and T_s can be associated by combining equation (1) and the Arrhenius type of function described in other literature [25–27]. The calibration function $T = T(R)$ is used to derive temperature from the intensity ratio during the measurement.

The calibration approach is also schematically presented in the following, taking the calibration done with deionized water and glass slice as an example. In figure 6, well-aligned $T_s(t)$ and $\overline{R}(t)$ are shown as blue and black curves, respectively. Intriguingly, the gradual decay of the baseline appears in the curve of $\overline{R}(t)$. This effect is caused by photobleaching, i.e. the gradual decay of the luminescence intensity with multiple exposures. A correction for such a decay is applied, and a detailed discussion can be found in the supplementary information. The corrected value is plotted as the orange curve in the same figure. For a certain time *t*, a certain $\overline{R}(t)$ and $T_s(t)$ can be paired. They are plotted as blue circles in figure 7. The fitted temperature calibration curve is given as the dark blue curve in this figure. The deviation between the measured temperature to the set temperature is also depicted as the orange crosses. They are scattering around 0 °C, showing that the measurement is unbiased. The standard deviation of 0.45 °C implies that a very low measurement uncertainty can be achieved.

Calibration measurements were repeated several times using different types of fluid, substrate, set temperature, and recording parameters to investigate relevant factors of the calibration approach. It was found that the set temperature and sampling rate have no impact on the calibration curve as expected, and good reproducibility can be achieved. In comparison, the calibration curve is sensitive to the type of fluid and substrate, as both affect the light transmission. Therefore, it is essential to keep both the same for the calibration and actual measurements. For the temperature measurement in the PDMS chamber of the SAW tweezer, the calibration curve obtained with a glycerol-water mixture with a weight ratio of 54.5% of glycerol and a LiNbO$_3$ substrate with the thickness of 0.5 mm was used.
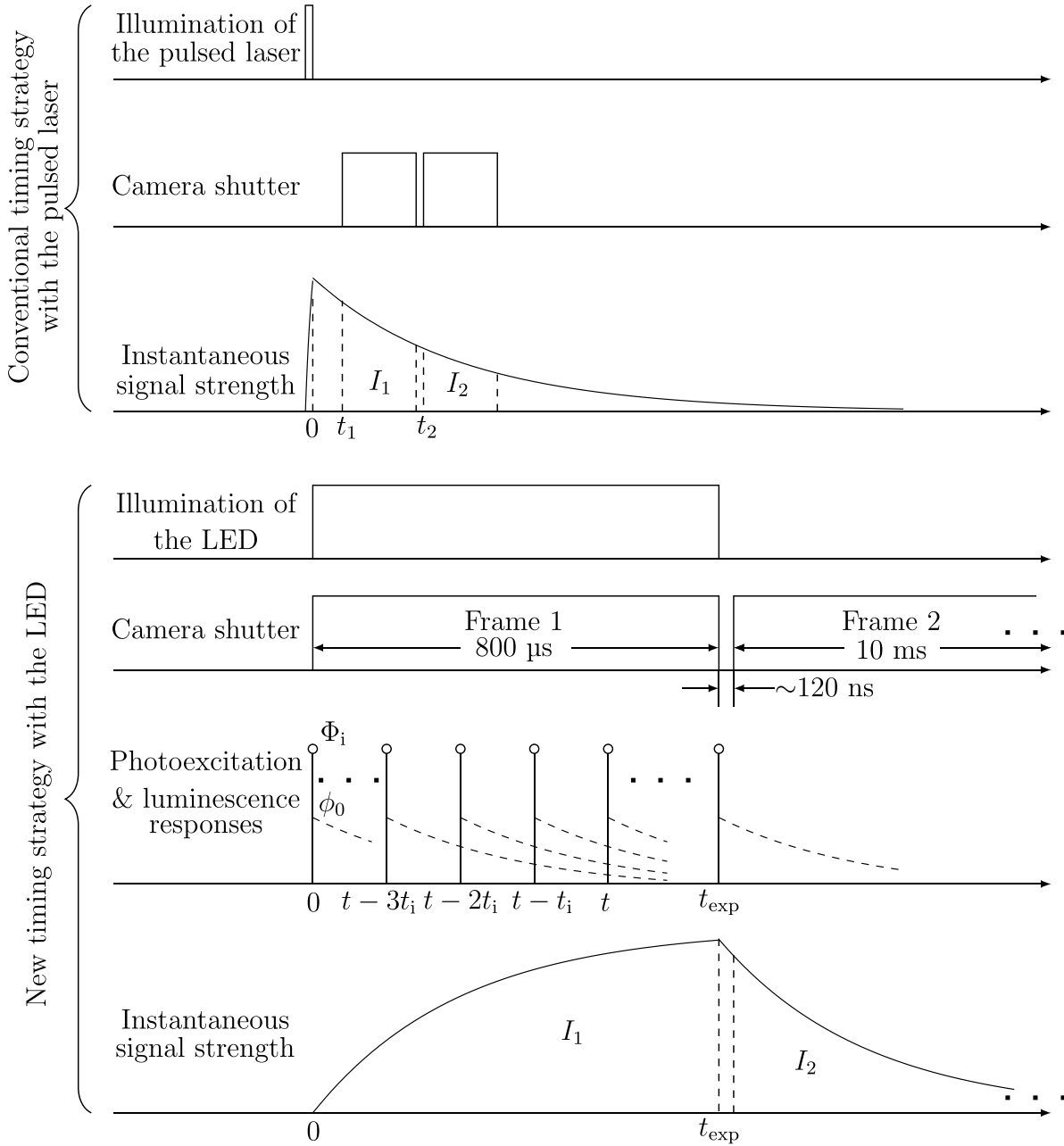
Figure 4. Comparison of the conventional timing schedule with the pulsed laser and the new one with the LED.

3. Reliability of the combined measurement

The combined measurement of the temperature and velocity brings in a new aspect to be considered: the measurement of temperature and velocity shall be independent of each other. However, since both of them are realized by the processing of the same particle image, there might be some dependency between them, jeopardizing the reliability of the combined measurement. In this section, we investigated the reliability of location measurement under varying temperatures and, conversely, the reliability of temperature measurement with the varying location of the tracer particle.

Furthermore, the much longer exposure time of both the first and second frames also means that the movement of tracer

particles will cause a more significant measurement error. We also considered this effect and defined limitations with respect to particle displacement, within which the measurement error is acceptable.

3.1. Reliability of location measurement under varying temperature

The data that was collected during the repeated calibration measurements mentioned in section 2.4 is suitable for investigating the reliability of the location measurement under varying temperatures. Assuming that the particles were settled on the substrate, the temporal fluctuation of the measured positions (denoted as $\epsilon_x, \epsilon_y, \epsilon_z$ in the following discussion) are good
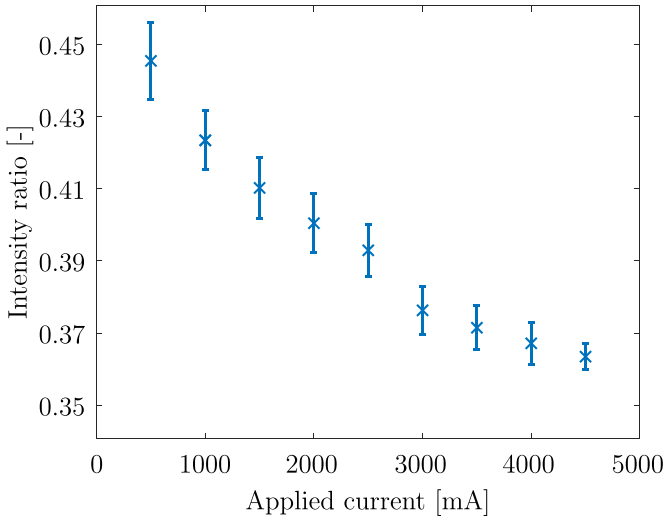
Figure 5. Dependency of the ensemble average intensity ratio on the applied current on the LED at a constant temperature of the fluid. The markers show the mean and the error bars represent the standard deviation.
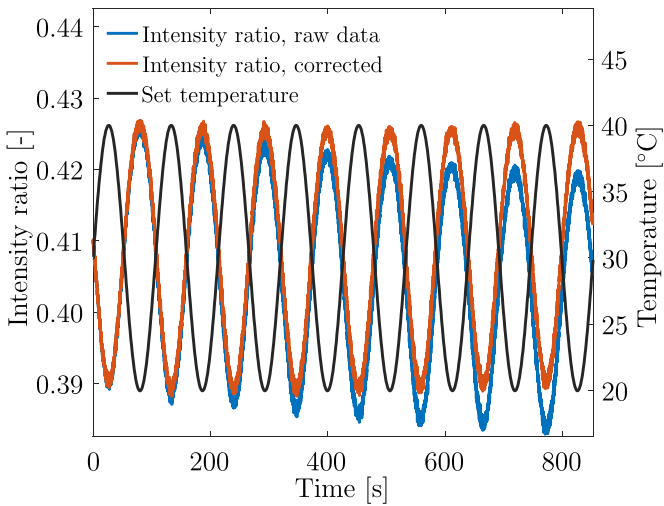

Figure 7. Experimental data for temperature calibration, the fitted calibration curve, and the deviation of the measured temperature.

Figure 6. Intensity ratio as a function of time before and after correction and the varying set temperatures.

Figure 8. Fluctuation of the measured *z*-coordinate with periodically varying temperature during calibration measurement.

indicators for the measurement uncertainties. There is no temporal variation on ϵ_x and ϵ_y, even though the set temperature varies over time. The standard deviation of them is about 0.06 μm and 0.2 μm in *x*- and *y*-directions, respectively, showing good robustness in the measurement of lateral coordinates against varying temperatures.

However, as can be seen in figure 8, ϵ_y decreases almost linearly with increased temperature. The Pearson correlation coefficient $\rho(\epsilon_z, T)$ as high as -0.93 again proved that they are inversely correlated. The slope was found to be $-0.15\ \mu\text{m}\,^\circ\text{C}^{-1}$ by means of linear regression. However, further measurement showed that it is just an artifact caused by the calibration stage. Detailed information is given in the supplementary. We found that at a higher temperature, additional pressure was exerted on the surface of the glass slice via the O-ring, causing the bending of the glass and thus the decreased
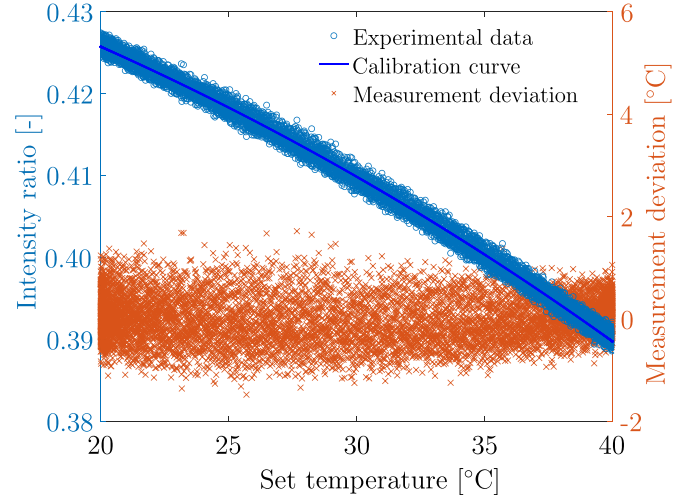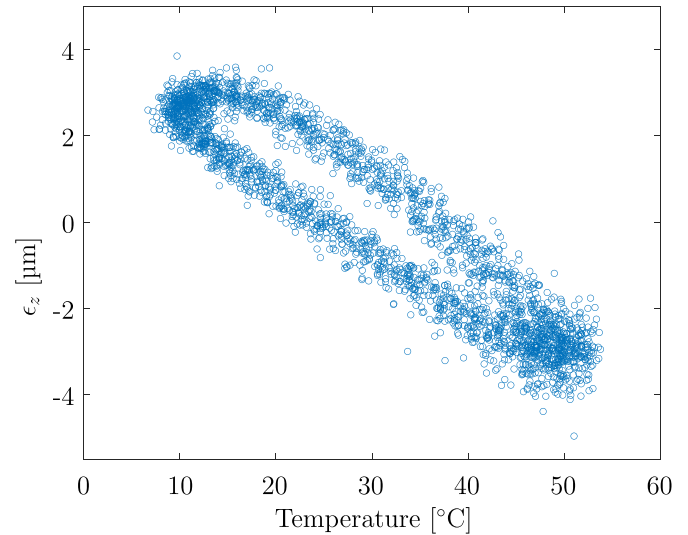
height. The force was caused by the thermal expansion of the Peltier element fixed on top of them. After the correction of this effect, the standard deviation of ϵ_y was estimated to be about 1.05 μm over the whole temperature range. It is close to the value obtained during the APTV calibration, implying good reliability of the *z*-coordinate measurement under varying temperatures. Nevertheless, all possible sources of errors during the real measurement have to be carefully evaluated.

3.2. Reliability of temperature measurement under varying location

To investigate the reliability of temperature measurement on the particle location, we fixed the set temperature at 30 °C traversed the microscope platform in *x*- and *y*-direction, and the objective lens in *z*-direction with steps of 200 μm, 200 μm, and 2.5 μm, respectively. In each position, one double-frame
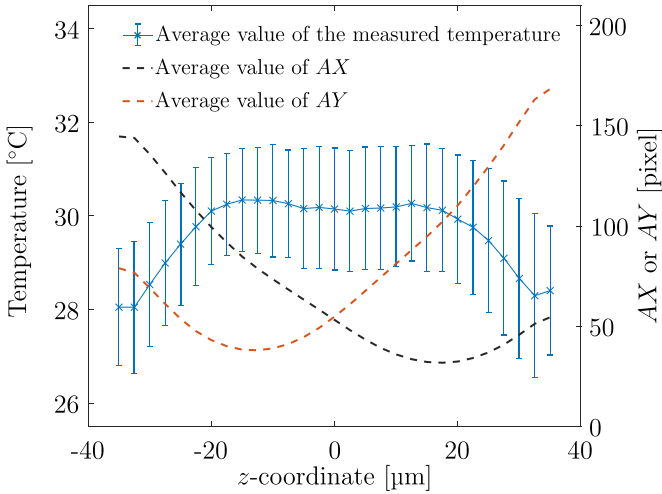
Figure 9. Dependency of the measured temperature and *AX*, *AY* on the *z*-location. Please note, the standard deviation of the measured temperature represented by the error bar includes also the uncertainty in different *x*- and *y*-locations.

Figure 10. Dependency of the measure temperature on the *xy*-locations.

image was recorded. In this way, we collected enough particle images with different relative locations to the measurement volume.

A certain dependency of the measured temperature on the *z*-location can be observed in figure 9. In this figure, data collected from all different traversed positions are shown. The average measured temperature of the particle images recorded at a certain traverse height is plotted as the blue curve with an error bar indicating the standard deviation. We can see that in the range of $|z| < 17.5\,\mu$m, the estimation of temperature is relatively robust. However, a gradual underestimation of the temperature exists beyond this range. The reason for that could be the increase of the particle image area and the resultant decreasing of I_1. Considering the change of *AX* and *AY* plotted as the dashed curve in this figure, within the range of $-12.5\,\mu$m $< z < 17.5\,\mu$m, the change on *AX* and *AY* along with the *z*-coordinate are opposite to each other, resulted in a relatively stable particle image area.

In figure 10, we considered only the measured temperatures in the reliable measuring range of height and plotted the measured temperature against the *x*- and *y*-coordinates. The underestimated temperature on the margin of the FOV leads to an uneven distribution of the measured temperature on the *xy*-plane. Regardless of the different traverse positions of the microscope platform and objective lens, it always has the shape of an elliptic paraboloid, which excludes the possibility that such a distribution exists physically, e.g. due to the heat transfer to the ambient. Therefore, it has to be an artifact caused by the optical system, which is similar to that reported by Massing *et al* [28] during the development of a temperature measurement method based on luminescent two-color tracer particles. The deviation was explained with the imperfection of optical lenses and filters, and further corrected by a second-order polynomial. After applying the same correction, the standard deviation of the measured temperature for individual particles within one recorded image was decreased from 1.3 °C to 1.0 °C and more importantly, the measured
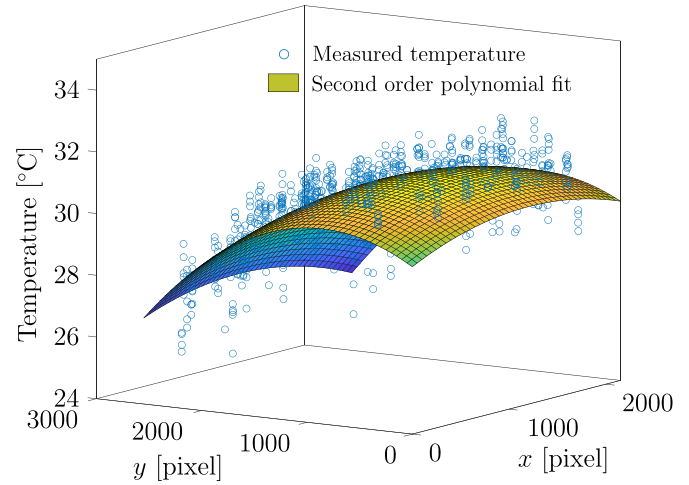
temperature was distributed evenly on the *xy*-plane with an average value of 29.8 °C, close to the ground truth value of 30 °C. Except for that, in our current research, the sensing area of the camera sensor is slightly larger than the FOV of the microscope. It leads to a rapid change in the illumination intensity on the margin of the image. Therefore, we shrank down the region of interest to exclude the particle images that are not adequately illuminated.

3.3. Measurement errors caused by the movement of tracer particles during the exposure

Not only the location of the tracer particle but also its time derivative, the particle's velocity, may influence the location and temperature measurement. Here we consider only the velocity components in *xy*-plane v_x and v_y. In the particle image captured in the first frame, the movement causes a drift of the centroid location and an elongation along the moving direction. The drift can be regarded as the deviation on the measurement of (x, y) during the location measurement. The elongation leads to the deviation on (AX, AY) and, therefore, can also cause bias in estimating the *z* location. Both the drift and the elongation make the grayscale distribution of the particle image deviate from the ideal 2D Gaussian distribution, leading to a measurement bias of *T*. Considering that in most cases the drift and the elongation are almost equal to each other, here we do not distinguish between them. The upper limit of them is the moving distance of the particle during the exposure of the first frame $\delta_{x,y}$, which can be estimated by the following equation:

$$\delta_x = \frac{t_{\exp}}{\Delta t}\Delta X = \frac{t_{\exp}}{M_x}v_x, \quad \delta_y = \frac{t_{\exp}}{\Delta t}\Delta Y = \frac{t_{\exp}}{M_x}v_x \quad (2)$$

where ΔX and ΔY are the displacements of the particle image in *x*- and *y*-direction in between subsequent images taken with a time difference Δt, and M_x, M_y are the scaling factors in *x*- and *y*-directions, respectively. It means that $\delta_{x,y}$ is linearly
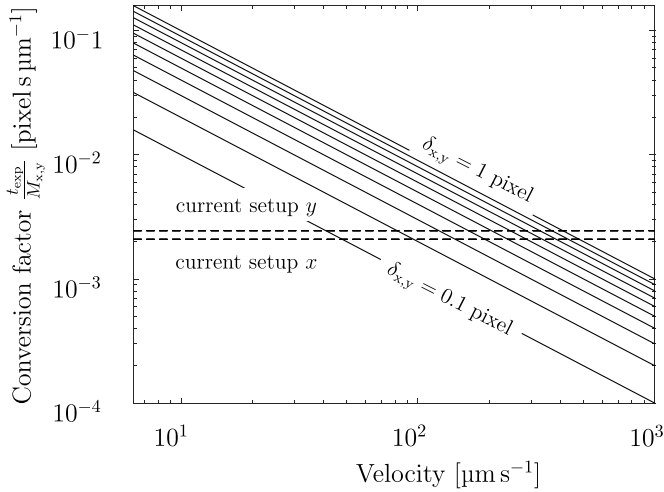
Figure 11. The required lowest conversion factor under different velocity using $\delta_{x,y}$ ranging from 0.1 pixel to 1 pixel as criteria, the step between two neighbouring curves is 0.1 pixel.

Figure 12. Temperature measured under different δ_y with the markers representing the average temperature and δ_y, and with the horizontally and vertically aligned error bars showing their standard deviation.

related to the corresponding velocity component with the conversion factor of $\frac{t_{\exp}}{M}$. With a given velocity, the lower the conversion factor, the smaller the moving distance. Similar to the analysis provided in some literature [29, 30], setting $\delta_{x,y}$ ranging from 0.1 pixel to 1 pixel as criteria, the required lowest conversion factor for different velocity to be measured is provided in figure 11. For the current setup, the conversion factor in both directions are also given as the dashed lines. Using 1 pixel of $\delta_{x,y}$ as the criterion, the upper limits of measurable v_x and v_y are around 480 µm s^{-1} and 410 µm s^{-1}, respectively.

As for the error on the measurement of the z-coordinate δ_z caused by $\delta_{x,y}$, it can be expressed as:

$$\delta_z = |z(AY, AY) - z(AX + \delta_x, AY + \delta_y)|. \tag{3}$$

Therefore, it is closely related to the sensitivity of z to the change of (AX, AY), which is depended on the setup and can be found in the APTV calibration curve. For our current setup, one unit pixel length of the error vector (δ_x, δ_y) can only lead to a δ_z less than 0.5 µm. Detailed calculation approach can be found in the supplementary information.

The investigation of the error caused by $\delta_{x,y}$ on the measurement of T was done by performing experiments on a pressure-driven channel flow inside the microchannel mentioned in section 2.2. A glycerol-water mixture was used to match the density of the particles and fluid. The particle suspension was driven by a syringe pump. Flow directions were aligned parallel either to x- or to y-direction. Pumping was started and stopped manually during the recording of images, such that for some specific particles, images were captured both when they were static and moving. With this arrangement, the temperature of the static particle images can be regarded as the ground truth, and in different measurement runs this value was stable and it is around 23.3 °C. Different ΔX and ΔY were obtained by changing the volume flow rate set on the syringe pump. The related $\delta_{x,y}$ were estimated with equation (2). Taking the results obtained in y-direction as an example, the mean value of the
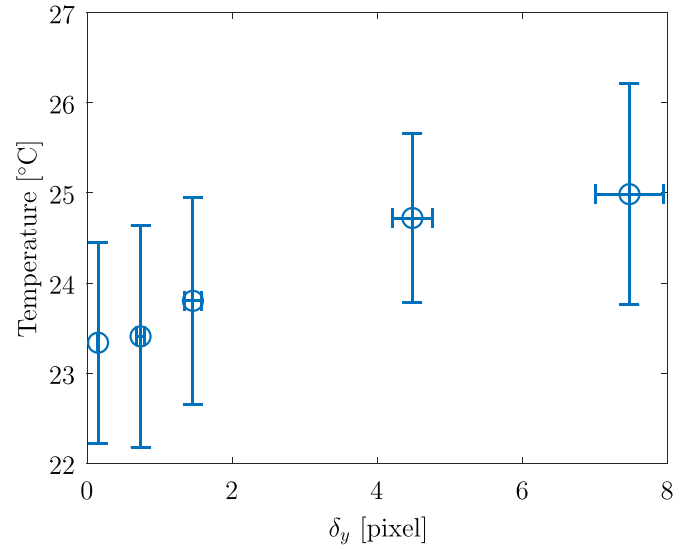
measured temperature and δ_y are plotted as circles in figure 12. The length of the error bar in vertical and horizontal directions gives the standard deviation of T and δ_y. From this figure, we can tell that with the increase of δ_y, the mean value of the measured temperature also slightly increased. However, the measurement of T can still be regarded as very robust against particle movement. Compared to the temperature measured with static particles, with the δ_y up to 7.48 pixels (meaning a ΔY of 935 pixels), the mean value of the measured temperature increased to 25.0 °C, representing a bias of only 1.7 °C.

All the errors mentioned above will become more significant with further increasing moving velocity or magnification. In this case the particle streak velocimetry might become more suitable [31].

4. Measurements on the SAW tweezer

The SAW tweezer can be regarded as a suitable showcase for the combined velocity and temperature measurement. During its operation, small objects in the microfluidic chamber can be manipulated spatially by the acoustic fields via either the acoustic radiation force or the viscous drag force until they were trapped at some specific locations. In the same time, due to the power imposed on the system by acoustic actuation, the temperature of the manipulated objects can increase. Hence, the temperature of the manipulated objects is crucial if they are temperature-sensitive biological samples. Therefore, we intended to measure the spatial movement and temperature of the particles simultaneously during the initial phase of trapping, to investigate this phenomenon in a more comprehensive manner.

However, as mentioned in the introduction, applying a conventional APTV & LLI measurement on the SAW tweezer, a significant heating effect was found due to the usage of the
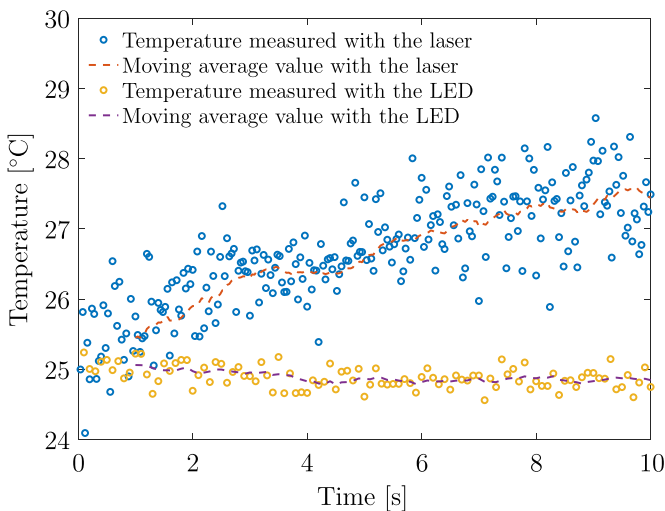
Figure 13. Temporal evolution of the temperature measured with the pulsed laser and with the LED in the PDMS chamber.

laser. In this measurement, tracer particles were suspended in a glycerol-water mixture and introduced into the chamber of the SAW tweezer. After several minutes of waiting time, they were sedimented on the substrate of the acoustic tweezer and their temperature was in equilibrium with the ambient. During the entire measurement, the SAW tweezer was not in operation. As the light source, an Nd:YAG laser with a pulse width of 5 ns, maximum pulse energy of 53 mJ (SpitLight Compact 100 PIV, Innolas GmbH) was operated under a fixed repetition rate of 25 Hz. A high-speed CMOS camera (Imager HS 4M, LaVision GmbH) was used to record image sequences. The timing for the laser and the camera followed the conventional arrangement depicted in the upper part of figure 4. The exposure time of both frames was 300 µs. About 62% of the maximum power of the laser (ca. 0.8 W) was used to realized the luminescence saturation of the dye, so that the highest signal-to-noise ratio can be guaranteed. As the result, the time-resolved spatial averaged temperature of the particles is shown in figure 13 as the blue circles. It increased by up to 2 K in 10 s. Since no acoustic waves were excited and no other source brought in energy to the SAW tweezer system, it is convincing that such an increase of temperature was induced by the laser.

Changing the measurement system to the one presented herein, we repeated the measurement with a comparable signal-to-noise ratio defined as the maximum grayscale divided by the standard deviation of the background noise. With the new timing schedule, the signal-to-noise ratio was found close to which obtained with the laser (ca. 43 vs. ca. 48). The LED was operated with the maximum instantaneous power of 4 W. With an illumination time of 800 µs and a repetition rate of 10 Hz, the time averaged power was 0.032 W, significantly lower that the power of the laser. As the result, the spatial averaged temperature was almost constant over time, as depicted by the yellow circles in figure 13. This clearly proves that the heating was avoided, using the LED and the new

timing strategy for illumination and exposure of the sCMOS camera operating in double frame mode. In addition, the smaller fluctuation of the measured temperature shows a lower measurement uncertainty.

With the circumvention of the light-source induced heating, we were able to conduct reliable measurements on the three-dimensional patterning and heating of particles trapped within the SAW tweezer mentioned above. A video demonstrating the whole trapping process, including the raw images and the reconstructed 3D locations and temperature of these particles, is provided as supplementary information. For further details about the entire experiments, results and conclusions that can be drawn for the use of SAW tweezer in biological applications, we refer to Deng *et al* [19] and Weser *et al* [20].

5. Discussion and summary

A crucial development in the conventional image-based simultaneous velocity and temperature measurement method, the APTV combined with luminescence lifetime imaging, is elaborated in this article. The pulsed laser and the high-speed CMOS camera are replaced by an LED and a low-speed double-frame camera, respectively. With a much reduced power, the heating caused by the laser is avoided. The lower power provided by the LED is counterbalanced by a vastly extended illumination time and the exposure time for both frames. Therefore, a high signal-to-noise ratio of the images can be obtained. The detailed implementation procedure and the measurement principle of this adapted measurement method are described. In addition, we proposed a novel calibration approach for the temperature measurement based on the periodic varying set temperatures and the matching of the corresponding intensity ratios, assuming an negative correlation between them. A constant delay between the set temperature logging and the image-based measurement is realized with this approach. The calibration is unbiased over the whole varying range of temperatures, with a low uncertainty of 0.45 °C resulting from random errors during the calibration measurement. Furthermore, the dependence of temperature and location measurements on each other was rigorously examined. With a systematic experimental investigation, we found that the location measurement is robust against the varying temperature, and the temperature measurement is very reliable in the center of the measurement volume. In addition, the measurement errors caused by the movement of tracer particles during the long illumination time are analysed. With the current measurement system, largest measurement biases caused by one pixel of particle shifting during the illumination are less than one pixel on the x- and y-locations, 0.5 µm on the z-location, and negligible on the temperature.

Compared with the conventional measurement configuration using a pulsed-laser as the light source, the new configuration has a lower measurement rate (25 Hz vs. 10 Hz) and brings in a new issue of particle movement during the long illumination and exposure time. Therefore, the measurable

range of the velocity is reduced. However, several advantages are gained, including lower cost on the hardware device, higher measurement precision, and most importantly, no heating effect. These new features make the new configuration especially suitable for measurement tasks in extremely tiny volumes of stagnant fluid, e.g. in microfluidics. As the costs for an LED and a low-speed double-frame camera are much lower than for a double-pulse high-power laser and a high-speed camera, the approach might be of broader use in different labs.

Data availability statement

All data that support the findings of this study are included within the article (and any supplementary files).

Acknowledgments

Conflict of interest

The authors declare no competing interest.

ORCID iDs

Zhichao Deng ⓘ https://orcid.org/0000-0001-6009-3104
Jörg König ⓘ https://orcid.org/0000-0002-7832-9223
Christian Cierpka ⓘ https://orcid.org/0000-0002-8464-5513

References

[1] Wu J, He Z, Chen Q and Lin J-M 2016 Biochemical analysis on microfluidic chips *TRAC Trends Anal. Chem.* **80** 213–31

[2] Ohno K-I, Tachikawa K and Manz A 2008 Microfluidics: applications for analytical purposes in chemistry and biochemistry *Electrophoresis* **29** 4443–53

[3] Günther A and Jensen K F 2006 Multiphase microfluidics: from flow characteristics to chemical and materials synthesis *Lab Chip* **6** 1487–503

[4] Karimi M, Bahrami S, Mirshekari H, Basri S M M, Nik A B, Aref A R, Akbari M and Hamblin M R 2016 Microfluidic systems for stem cell-based neural tissue engineering *Lab Chip* **16** 2551–71

[5] Miralles V, Huerre A, Malloggi F and Jullien M-C 2013 A review of heating and temperature control in microfluidic systems: techniques and applications *Diagnostics* **3** 33–67

[6] Massing J, van der Schoot N, Kähler C J and Cierpka C 2019 A fast start up system for microfluidic direct methanol fuel cells *Int. J. Hydrog. Energy* **44** 26517–29

[7] Massing J, Mutschke G, Baczyzmalski D, Hossain S S, Yang X, Eckert K and Cierpka C 2019 Thermocapillary convection during hydrogen evolution at microelectrodes *Electrochim. Acta* **297** 929–40

[8] Wiklund M 2012 Acoustofluidics 12: biocompatibility and cell viability in microfluidic acoustic resonators *Lab Chip* **12** 2018–28

[9] Shilton R J, Mattoli V, Travagliati M, Agostini M, Desii A, Beltram F and Cecchini M 2015 Rapid and controllable digital microfluidic heating by surface acoustic waves *Adv. Funct. Mater.* **25** 5895–901

[10] Abram C, Fond B and Beyrau F 2018 Temperature measurement techniques for gas and liquid flows using thermographic phosphor tracer particles *Prog. Energy Combust. Sci.* **64** 93–156

[11] Someya S 2021 Particle-based temperature measurement coupled with velocity measurement *Meas. Sci. Technol.* **32** 042001

[12] Dabiri D 2009 Digital particle image thermometry/velocimetry: a review *Exp. Fluids* **46** 191–241

[13] Brites C D, Balabhadra S and Carlos L D 2019 Lanthanide-based thermometers: at the cutting-edge of luminescence thermometry *Adv. Opt. Mater.* **7** 1801239

[14] Massing J, Kähler C J and Cierpka C 2018 A volumetric temperature and velocity measurement technique for microfluidics based on luminescence lifetime imaging *Exp. Fluids* **59** 1–13

[15] Cierpka C and Kähler C J 2012 Particle imaging techniques for volumetric three-component (3D3C) velocity measurements in microfluidics *J. Vis.* **15** 1–31

[16] Cierpka C, Rossi M, Segura R and Kähler C J 2010 On the calibration of astigmatism particle tracking velocimetry for microflows *Meas. Sci. Technol.* **22** 015401

[17] Ballew R M and Demas J N 1989 An error analysis of the rapid lifetime determination method for the evaluation of single exponential decays *Anal. Chem.* **61** 30–33

[18] Abram C, Panjikkaran I W, Ogugua S N and Fond B 2020 ScVO$_4$:Bi^{3+} thermographic phosphor particles for fluid temperature imaging with sub-$^{\circ}$C precision *Opt. Lett.* **45** 3893–6

[19] Deng Z, Kondalkar V, Weser R, Schmidt H, Cierpka C and König J 2021 Experimental investigations of a SAW system for parallel analysis of single cells *Experimentelle Strömungsmechanik: 28. Fachtagung* vol 35 (German Association for Laser Anemometry GALA e.V.)

[20] Weser R, Deng Z, Kondalkar V V, Darinskii A N, Cierpka C, Schmidt H and König J 2022 Three-dimensional heating and patterning dynamics of particles in microscale acoustic tweezers *Lab Chip* **22** 2886–901

[21] Basu B B J and Vasantharajan N 2008 Temperature dependence of the luminescence lifetime of a europium complex immobilized in different polymer matrices *J. Lumin.* **128** 1701–8

[22] Cierpka C, Rossi M, Segura R, Mastrangelo F and Kähler C J 2012 A comparative analysis of the uncertainty of astigmatism-μPTV, stereo-μPIV and μPIV *Exp. Fluids* **52** 605–15

[23] König J, Chen M, Rösing W, Boho D, Mäder P and Cierpka C 2020 On the use of a cascaded convolutional neural network for three-dimensional flow measurements using astigmatic PTV *Meas. Sci. Technol.* **31** 074015

[24] Greben M and Valenta J 2020 Power-dependent photoluminescence decay kinetics of silicon nanocrystals under continuous and pulsed excitation *Faraday Discuss.* **222** 274–93

[25] Borisov S M and Wolfbeis O S 2006 Temperature-sensitive europium (III) probes and their use for simultaneous luminescent sensing of temperature and oxygen *Anal. Chem.* **78** 5094–101

[26] Liebsch G, Klimant I and Wolfbeis O S 1999 Luminescence lifetime temperature sensing based on sol-gels and poly(acrylonitrile)s dyed with ruthenium metal–ligand complexes *Adv. Mater.* **11** 1296–9

[27] Peng H, Stich M I, Yu J, Sun L-N, Fischer L H and
     Wolfbeis O S 2010 Luminescent europium (III)
     nanoparticles for sensing and imaging of temperature in the
     physiological range *Adv. Mater.* **22** 716–9

[28] Massing J, Kaden D, Kähler C J and Cierpka C 2016
     Luminescent two-color tracer particles for simultaneous
     velocity and temperature measurements in microfluidics
     Meas. Sci. Technol. **27** 115301

[29] Cierpka C, Hain R and Buchmann N A 2016 Flow
     visualization by mobile phone cameras *Exp. Fluids*
     57 1–10

[30] Hain R and Kähler C J 2007 Fundamentals of multiframe
     particle image velocimetry (PIV) *Exp. Fluids* **42** 575–87

[31] Fan L, Vena P, Savard B, Xuan G and Fond B 2021
     High-resolution velocimetry technique based on the
     decaying streaks of phosphor particles *Opt. Lett.* **46** 641–4